IEEE Photonics Journal
An IEEE Photonics Society Publication

Monolithic InP 100-Channel × 10-GHz Device for Optical Arbitrary Waveform Generation

Volume 3, Number 6, December 2011

Francisco M. Soares
Nicolas K. Fontaine, Member, IEEE
Ryan P. Scott, Member, IEEE
J. H. Baek
X. Zhou
T. Su
S. Cheung
Y. Wang
C. Junesand
S. Lourdudoss
K. Y. Liou
R. A. Hamm
W. Wang
B. Patel
L. A. Gruezke
W. T. Tsang
Jonathan P. Heritage, Fellow, IEEE
S. J. B. Yoo, Fellow, IEEE

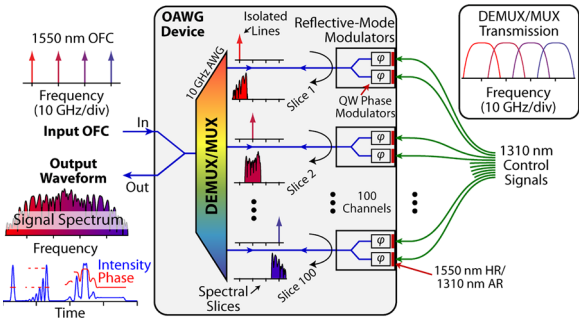

DOI: 10.1109/JPHOT.2011.2170558
1943-0655/$26.00 ©2011 IEEE

IEEE photonics SOCIETY

IEEE

Monolithic InP 100-Channel × 10-GHz Device for Optical Arbitrary Waveform Generation

Francisco M. Soares,[1,4] Nicolas K. Fontaine,[1] *Member, IEEE*, Ryan P. Scott,[1] *Member, IEEE*, J. H. Baek,[1,5] X. Zhou,[1] T. Su,[1] S. Cheung,[1] Y. Wang,[1] C. Junesand,[2] S. Lourdudoss,[2] K. Y. Liou,[3] R. A. Hamm,[3] W. Wang,[3] B. Patel,[3] L. A. Gruezke,[3] W. T. Tsang,[3] Jonathan P. Heritage,[1] *Fellow, IEEE*, and S. J. B. Yoo,[1] *Fellow, IEEE*

[1]Department of Electrical and Computer Engineering, University of California, Davis, CA 95616 USA
[2]Department of Microelectronics and Information Technology, KTH Royal Institute of Technology, 16440 Kista, Sweden
[3]Multiplex, Inc., South Plainfield, NJ 07080 USA
[4]Fraunhofer Heinrich Hertz Institute, 10587 Berlin, Germany
[5]Samsung Electronics, Hwasung-City 445-701, Korea

DOI: 10.1109/JPHOT.2011.2170558

Manuscript received September 22, 2011; accepted September 26, 2011. Date of publication October 3, 2011; date of current version November 1, 2011. This work was supported in part by The Defense Advanced Research Projects Agency and Space and Naval Warfare Systems Command under Optical Arbitrary Waveform Generation Contract HR0011-05-C-0155 and by the National Science Foundation under Electrical, Communications and Cyber Systems Grant 1028729. Corresponding authors: R. P. Scott and S. J. B. Yoo (e-mail: rpscott@ucdavis.edu; sbyoo@ucdavis.edu).

Abstract: We demonstrate monolithic integration of a 100-channel arrayed-waveguide grating (AWG) with 10-GHz channel spacing and 100 optically controlled Michelson-interferometer-based phase and amplitude modulators. The high-resolution AWG showed better than −15-dB crosstalk, and the modulator extinction ratio was better than 20 dB with either electrical or optical modulation control. The twin-integrated devices comprise a 50-mm diameter InP wafer with 1200 independent optoelectronic components.

Index Terms: Integrated optoelectronics, optical device fabrication, optical modulation, optical pulse shaping.

1. Introduction

Manipulation of the amplitude and phase of a stable optical frequency comb (OFC) on a line-by-line basis enables a powerful class of pulse shaping known as optical arbitrary waveform generation (OAWG) [1]–[3]. Potential applications of OAWG include optical communications and arbitrary radio-frequency (RF)/microwave waveform generation. Most previous work [4], [5] has concentrated on static-OAWG, where the waveform shaper utilized slow modulators to adjust the amplitude and phase of each comb line. The lines are coherently recombined using spectral multiplexers (MUXs) with narrow passbands. These waveform shapers are essentially configurable, high-resolution optical filters and thus the output waveform is repetitive. When trying to rapidly update (i.e., each pulse of the OFC) the modulations of a typical static-OAWG system, it has been shown that there is an inherent tradeoff between update speed and waveform fidelity [6], [7]. As a solution to this problem, we recently proposed spectral-slice dynamic-OAWG [8], [9], which is a technique to achieve

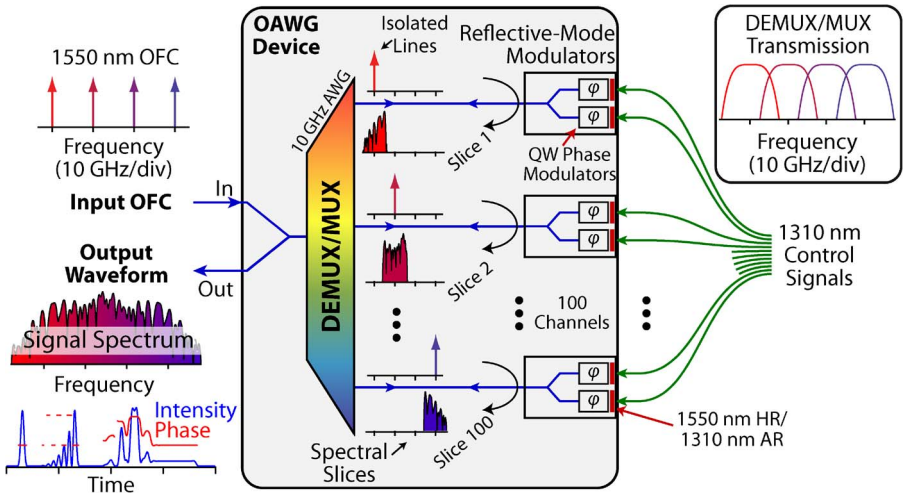

Fig. 1. Spectral-slice dynamic-OAWG using a reflective-mode device.

high-fidelity, continuous generation of arbitrary optical waveforms of scalable bandwidth using OFCs, spectral MUXs, and an array of modulators.

Although we recently demonstrated spectral-slice dynamic-OAWG using fiber-pigtailed devices [10], practical dynamic-OAWG implementations require a stable phase relationship between the spectral slices, and this necessitates an integrated, and preferably monolithic, platform that provides high-speed optical modulators and high-resolution spectral MUXs. Previously, our group reported a 10-channel, 10-GHz spacing InP-based OAWG device which utilized electrooptic modulation [11]. This paper describes and characterizes a monolithically integrated InP OAWG device with 100 channels spaced at 10 GHz for generating waveforms with up to 1 THz of optical bandwidth in the 1.55-μm telecommunications band. Electrooptic intensity and phase modulation of 100 channels at gigahertz rates is impractical due the sheer number of modulators and the inevitable RF crosstalk and electrical losses of the long transmission lines. Therefore, this paper discusses an integrated optical device which incorporates quantum-well (QW)-based phase modulators which are optically controlled (i.e., cross-phase modulation via free-carrier effects) by the intensity of remote, fiber-pigtailed 1310-nm or 1060-nm lasers. Measurements of the OAWG device show exceptionally low (-15 dB) crosstalk for a high-resolution, InP-based spectral MUX and show that the all-optical modulators are capable of greater than 1-GHz bandwidths.

2. Concept and Implementation

Fig. 1 illustrates how an input OFC is transformed into a target waveform using a reflective-mode spectral-slice dynamic-OAWG device where a single arrayed-waveguide grating (AWG) acts as both the spectral demultiplexer (DEMUX) and MUX. After demultiplexing the input OFC to separate waveguides, each isolated line undergoes independent modulation to create a slice of the target waveform's spectrum. Optical control signals (1310 nm or 1060 nm) drive the reflective-mode modulators (i.e., Michelson interferometers) through the high-reflection/antireflection (HR/AR) coated right facet (HR at 1550 nm, AR at 1310 nm). Push–pull type modulation is applied to each arm of the Michelson structure to create amplitude changes on that channel, while applying the same modulation to each arm generates phase changes. The MUX coherently combines the modulated lines (now spectral slices) into a single contiguous complex spectrum that exactly matches the target waveform. Key to high-fidelity OAWG device operation is high adjacent channel isolation (i.e., low crosstalk) for the MUX and overlapping passbands for the DEMUX. The upper right corner of Fig. 1 shows an example MUX transmission that accomplishes both requirements. Details of the spectral-slice dynamic-OAWG technique are discussed in [8] and [9].

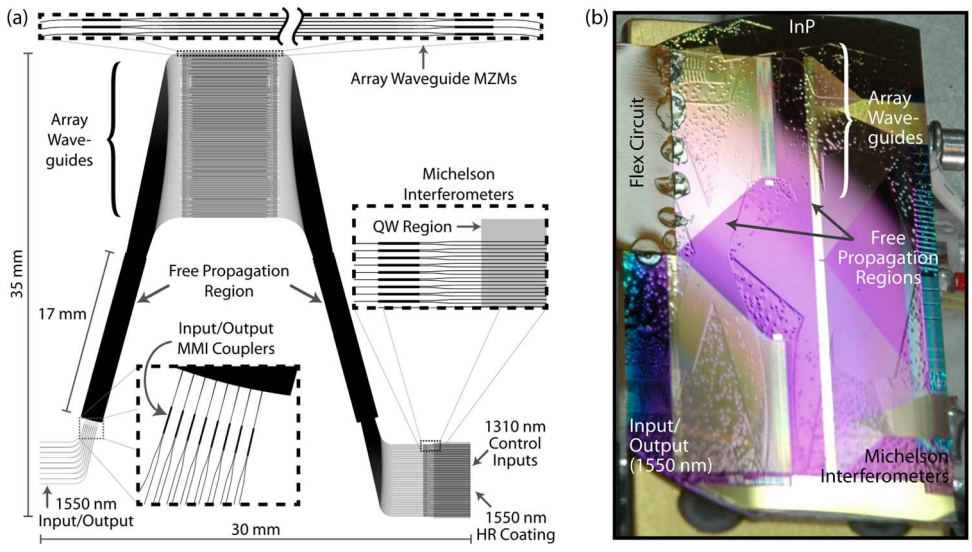

Fig. 2. (a) Mask layout of a single 100-channel × 10-GHz OAWG device. (b) Two fabricated InP devices from a single 50-mm diameter wafer with a flex circuit attached to one device.

Fig. 2(a) shows the waveguide mask layout of the InP OAWG device with overall dimensions of 30 mm × 35 mm, and Fig. 2(b) shows a photo of the fabricated device where two devices have been fabricated on a single 50-mm diameter wafer (upper device is a mirror image of the lower device). The device's cleaved-facet left side uses a multimode-interference (MMI) 2 × 1 coupler as the 1550-nm input and output. The AWG contains 400 arrayed waveguides and, as the upper detail in Fig. 2(a) shows, each has an electrooptic Mach–Zehnder modulator (MZM). High-resolution AWGs are extremely sensitive to phase perturbations in the arrayed waveguide; therefore, the MZMs provide both phase-error correction [12] and passband shaping [13] to achieve the desired passband isolation and overlap. (This is different from the device we reported in [14], where the AWG was designed to have a flat-top transmission by adding a parabolic taper at the AWG inputs and narrow waveguides at the AWG outputs.) Finally, each of the 100 AWG outputs has a Michelson interferometer consisting of a 2 × 1 MMI splitter/combiner, as shown on the right side detail in Fig. 2(a). The interferometer arms have a 1-mm-long QW phase modulator and an HR/AR-coated cleaved-facet mirror (reflectivity is 86% at 1550 nm, 6% at 1310 nm). The QWs have a photoluminescence (PL) peak at 1490 nm, and our epitaxial layer stack is designed to achieve phase modulation by two different methods: either by exploiting the electrooptic effect and applying a reverse bias voltage to the QW modulator or by injecting 1310-nm control light at the HR-facet side (see Fig. 1). Either the QWs or the wave-guiding core layer made of InGaAsP with a band gap at 1.15 μm (1.15Q) absorb the control light to induce cross-phase modulation via the plasma dispersion effect [15] due to the generated free carriers. For some devices that do not have QWs, a shorter wavelength control light at 1060-nm is used since it is more efficiently absorbed in the wave-guiding core layer.

3. Fabrication

The InP device fabrication process contains three epitaxial growth steps. The first step defines a 150-nm p-doped InP layer, a 212-nm 12-QW layer, a 0.5-μm n-doped Q(1.15) waveguide core layer, and a 2-μm n-doped buffer layer. The 12 QW layers consist of 12 quaternary wells and 13 quaternary barriers ($\sim$1490 nm PL peak). Subsequently, we pattern the QW layers in the modulator regions shown in Fig. 2 by using lithography and wet-chemical etching. The second epitaxial growth creates a 2-μm p-doped InP top-cladding layer followed by a 100-nm p-doped InGaAs layer. After photolithographically defining the waveguides, they are etched in a Br_2/N_2

reactive-ion-etcher using a 550-nm SiO_2 layer as a mask. The third growth step creates Fe-doped semi-insulating InP laterally by low-pressure hydride vapor phase epitaxy (HVPE) on the side of the etched waveguides. Afterwards, we deposit a 350-nm SiO_2 layer and define via contact openings to the QW phase modulators in the Michelson interferometers and the phase-error-correction modulators in the AWs. Finally, we pattern the metal layer on the topside of the wafer using lithography and lift-off and subsequently perform the backside metallization. Two OAWG devices are fabricated on each 50-mm InP wafer by overlaying the slab regions of the AWGs in a mirror image or by nesting one device below the other. The wafer-scale twin OAWG chip includes 1200 independently addressable optoelectronic components monolithically integrated.

A key challenge associated with large channel count OAWG devices is efficiently establishing the sheer number of electrical and optical connections to the device. The 100-channel OAWG device requires application of up to 400 DC voltages: 200 for AWG phase-error correction and/or passband shaping and 200 for biasing the Michelson interferometers. To avoid manually wire bonding so many connections, we developed a process to bond flex circuits to the InP device using a technique similar to flip-chip bonding. Metallization on the InP OAWG device [see Fig. 2(b)] includes two separate connection areas that consist of 200 gold bond pads arranged in two staggered rows with a 200-μm center-to-center spacing. A corresponding set of 200 solder bumps are arranged on one end of the flex circuit (via connect solder bumps to the copper traces), and the other end of the flex circuit is attached to a printed circuit board with header connectors that provide standard ribbon cable connections. The 200 optical connections for driving the Michelson-interferometer modulators with control light (see the right side of Fig. 2) are supplied by a custom fan-out silica planar lightwave circuit (PLC). By using the silica PLC, each InP OAWG device does not need its own large fiber array mated directly to the device. Instead, the silica PLC is moved from one InP device to another as necessary for testing.

4. Device Characterization

The complex (i.e., amplitude and phase) transmission characteristics of the 100-channel × 10-GHz OAWG device were measured using an optical vector network analyzer (OVNA) [16]. The OVNA employs polarization-sensitive, swept-wavelength interferometry to measure the transfer function of a device under test with only a single scan of a fast-sweeping tunable laser. The advantages of using the OVNA are high optical spectral resolution (100 MHz here), the ability to measure both the amplitude- and phase response of the device (which is essential for phase-error correction of the AWG), and a high dynamic range due to its balanced detection. Although the OAWG device supports propagation of both quasi-transverse-electric (TE) and quasi-transverse-magnetic (TM) polarizations, full functionality is only available with the TE polarization. This arises since only the TE polarization is influenced by the linear electrooptic effect for a vertical electric bias field when the crystal symmetry of InP is in the (001) orientation. Additionally, most devices within the OAWG chip, including the MMI couplers and QW modulators, were optimized for TE polarization. It was relatively simple to ensure a single polarization since the waveguide birefringence causes the AWG's spectral response to be significantly different for the two polarizations.

A key to the successful operation of the OAWG device is the performance of the AWG, which includes having low channel crosstalk. This requires that the high-resolution AWG's long array waveguides [see Fig. 2(a)] have precisely the correct length (i.e., the optical phases are matched). Any undesired difference in the total optical phase between the array waveguides is referred to as a phase error. Fig. 3 shows the measured phase error for each of the array waveguides (arms) within the AWG before (red dot) and after (blue dot) phase-error correction. For clarity, the rapid (from one waveguide to the next) phase fluctuations have been suppressed to show the slow fluctuations which are important for the AWG performance, and only the array waveguides with significant power are shown. Ideally, the phase would be flat across all of the array waveguides. However, phase errors are caused by practical fabrication limitations, such as variations in the core-layer composition and thickness and fluctuations in the waveguide width. Since the OVNA update rate is several hertz, it was possible to correct the phase errors in real-time. Thus, as the AWG phase

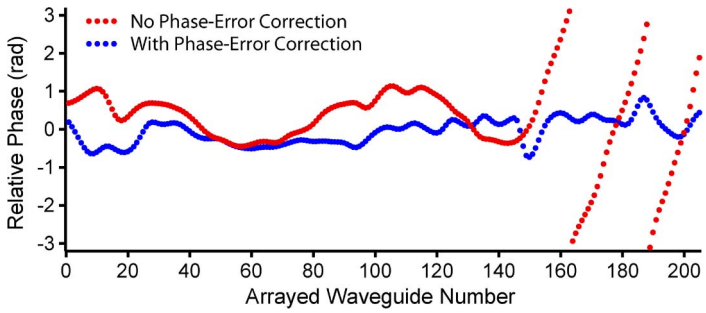

Fig. 3. Measured phase of the array waveguides (arms) in the 100-channel × 10-GHz AWG before and after phase-error correction.

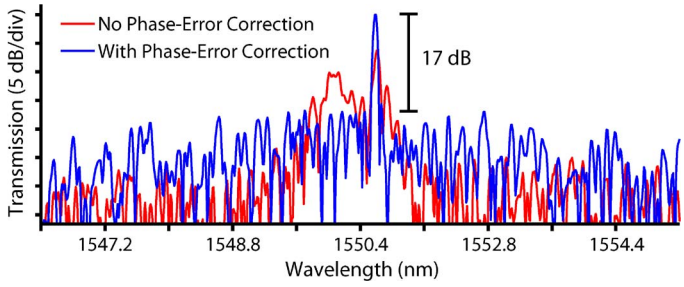

Fig. 4. Relative single-pass AWG transmission for a single output channel before (red) and after (blue) phase-error correction.

errors where measured, we used an array of inexpensive digital-to-analog converters (DACs) to apply the necessary reverse-bias voltages ($<$ 10 V) via the flex circuit to each array waveguide that needed a phase adjustment. This process was manual and iterative, but it was typically accomplished within 10s of minutes for the 200 array waveguides. Since the reverse-biased diode draws only a small amount of leakage current (several microamperes), this type of electrooptic phase-error correction requires little power. A 4-mm long InGaAsP/InP waveguide with a 1.5-μm thick depletion region typically requires less than 8 V of reverse bias for a 2π rad phase change. As Fig. 3 shows, the phase before correction has significant fluctuations and a large amount of linear phase in the array waveguides with a higher number (these are the longer waveguides). Before correction, the standard deviation of the phase errors is 1.03 rad, and after correction, the standard deviation drops to 0.33 rad. Most significantly, the linear phase has been removed, and the slowly varying phase errors are reduced. It is this reduction of phase errors in the AWG that improves the crosstalk performance of all 100 output channels simultaneously.

The improvement in AWG performance that follows a reduction in phase errors is most apparent when looking at the AWG transmission for a single channel in the frequency (wavelength) domain. Fig. 4 shows the single-pass AWG transmission measured with the OVNA for a single AWG output channel (#12) before and after phase-error correction. Without phase-error correction, the shape of the AWG passband is very broad, i.e., not single-peaked, and has a poor crosstalk level of -5 dB. After phase-error correction, it displays a -17 dB adjacent-channel crosstalk (this is especially good for such a high-resolution AWG). To remove the need for individual phase-error correction voltages and the external electrical connections it requires, it is possible to apply the same voltage to all of the electrodes and then trim the length of individual electrodes to set the phase-error correction. Alternatively, ion implantation may be used to induce material index changes [17] and achieve permanent phase-error correction.

Fig. 5 shows the measured single-pass AWG transmission for all 100 AWG outputs after phase-error correction (TE polarization). The data were taken by moving a fiber to each AWG output

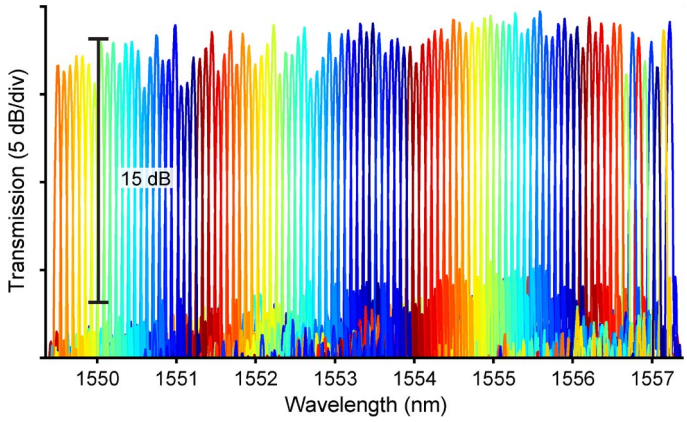

Fig. 5. Single-pass 100-channel × 10-GHz AWG transmission after phase-error correction.

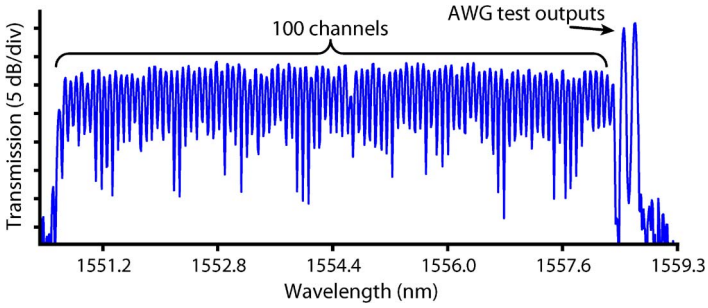

Fig. 6. Input to output transmission of the full 100-channel × 10-GHz OAWG device with no electrical or optical control signals present.

channel and making a measurement with the OVNA. The data show that none of the outputs are missing and that the average channel bandwidth is 6 GHz. The calculated crosstalk values (i.e., taken from the transmission peak to the largest subpeak, whether from the background or an adjacent channel) are as follows: −17.7 dB (best), −11.5 dB (worst), and −15.1 dB (average) with a 1.2-dB standard deviation for the average value. The output amplitude is relatively constant (1.0-dB standard deviation) if we consider expected variations in coupling when moving the fiber across the AWG output channels.

Fig. 6 shows the OAWG-device transmission measured with the OVNA with all 100 channels distinguishable after a round trip through the device (TE polarization). The two peaks on the long wavelength side are from AWG test outputs and are not part of the 100-channel response. Since there are no control signals present, the Michelson interferometers have random attenuations. Using straight waveguide samples cleaved from the same wafer and the Fabry–Pérot resonance method, we estimated the waveguide loss at 1.7–2 dB/cm (∼1 dB/cm is from doping p- and n-types for the p-n junction). The round-trip insertion loss of the OAWG device at a channel peak was typically ∼43 dB (TE polarization), which is consistent with the ∼11 cm round-trip path through the device, 2 × 3 dB loss for the MMI input/output coupler, and 2 × 6 dB of coupling loss from the lensed fibers. The average optical input powers were kept below +25 dBm to minimize the risk of damaging the input facet.

Fig. 7 shows the DC performance of the OAWG device for a typical channel as measured by the OVNA (other tested channels showed similar performance). Fig. 7(a) shows the transmission of channel #92 (TE polarization) while electrically biasing the QW phase modulator at three different voltages (0 V, −3 V, −6 V) in one arm of the Michelson interferometer. It demonstrates 20 dB of intensity modulation without affecting the transmission of the adjacent channels. Fig. 7(b) shows the

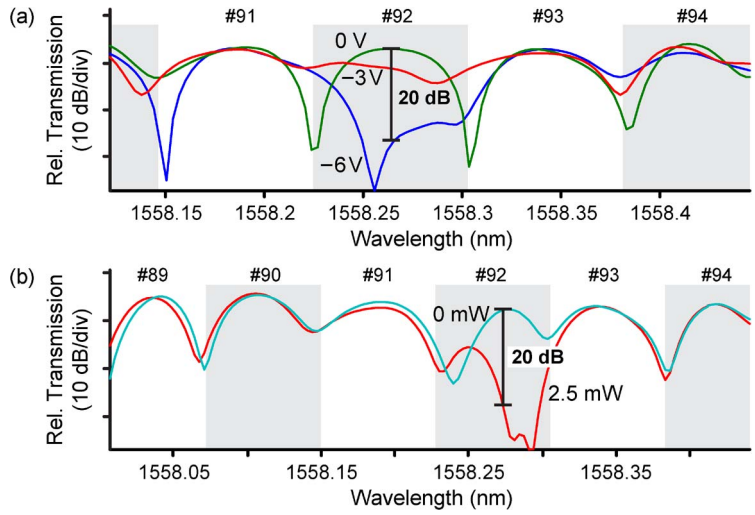

Fig. 7. Single channel extinction of the 100-channel × 10-GHz OAWG device for (a) electrical control and (b) 1310-nm optical control.

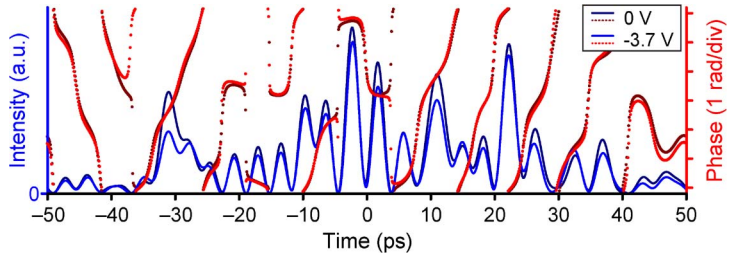

Fig. 8. Intensity (blue) and phase (red) of the output optical waveform for two different DC bias voltages on a single channel.

transmission while injecting a 1310-nm optical control signal into the same channel to observe the cross-phase modulation (at −3 V bias) using the Michelson's response. There is 20 dB of intensity modulation between the two different injected optical powers, i.e., 0 mW and 2.5 mW, and little observable crosstalk. Since the QW region was long compared with the control signal absorption length, the polarization of the control signal did not influence the modulator's response.

As a simple first demonstration of waveform shaping with this device, we injected a 26 line × 10-GHz input OFC that was produced by applying strong modulation to a cw laser with a phase modulator and a dual-electrode MZM [3], [18]. The repetitive output waveform was measured with no control signals applied. Then, we adjusted the DC bias on a single channel to observe the change in the output waveform. The low optical power (−20 dBm) out of the OAWG device required that we use four-quadrature spectral interferometry (FQSI) [19], which is a very sensitive coherent measurement technique. FQSI with balanced detection provides both the amplitude and phase of the waveform when it is measured against a well-characterized reference OFC (same as the input OFC here). Fig. 8 shows the temporal intensity and phase of the waveform for the two different bias voltages on Channel #92. Since only one channel out of the 26 that are illuminated is changing phase, we do not expect to see a large difference in the two waveforms. However, there is a distinctive difference between the two waveforms, and it is verifiable in the spectral domain.

To verify that only a single channel's phase is changed, we take the difference between the measured spectra at 0 V and −3.7 V bias and plot it in Fig. 9. Each dot represents the phase change for each of the 26 comb lines and only the controlled channel has a significant (∼3 rad)

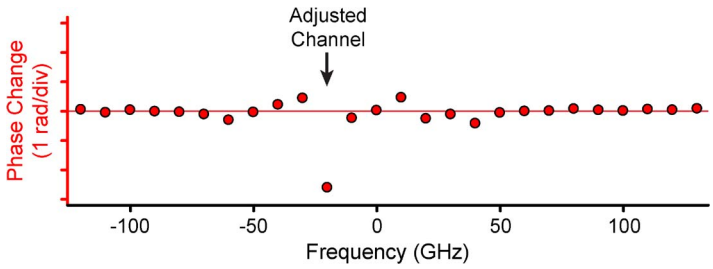

Fig. 9. Change in the phase of the optical waveform's spectrum for two different DC electrical biases on a single channel.

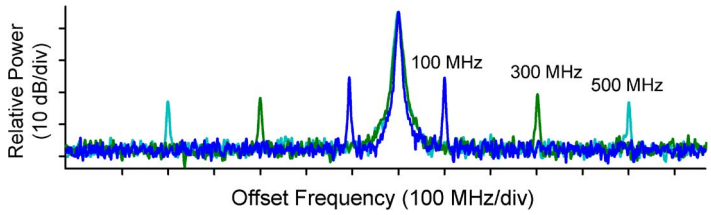

Fig. 10. Optical heterodyne measurement of the phase modulation sidebands at three different modulation frequencies created on a single comb line (∼1553.5 nm) by injecting a 1310-nm control signal with sinusoidal modulation into a QW phase modulator.

phase difference. The other channels do change some, possibly due to some crosstalk, but there were also some variations and drift during each measurement independent of changes in the bias voltage.

As an initial characterization of the dynamic response of the OAWG device using optical-optical modulation, we investigated the relative amplitude of the phase modulation sidebands created by a single QW phase modulator at different modulation frequencies. The measurement was performed by combining the 1310-nm control light and a single comb line (∼1553.5 nm, TE polarization) into a single fiber and injecting it into one arm of the Michelson interferometer on a center channel [see the right side of Fig. 2(a)] and then making an optical heterodyne measurement of the phase-modulated comb line after it exits the OAWG device [see the left side of Fig. 2(a)]. Fig. 10 shows the relative amplitude of the phase modulation sidebands for three different sinusoidal modulation frequencies of the 1310-nm control signal (2-mW peak power). At 100 MHz, the carrier-to-sideband amplitude is approximately −20 dBc, indicating a peak phase modulation index of ∼0.2 rad. As the modulation frequency was increased to 300 MHz and then 500 MHz, the sideband amplitudes dropped by 6 dB and 7 dB, respectively. Therefore, it was important to seek ways to improve the high-speed modulation response.

The high-speed performance of the optically driven modulators is determined primarily by the dynamics of the plasma dispersion effect. In multiple QWs, the phase modulation is increased because of the step-like density of states [15], and the modulation depth is mostly independent of the modulator length since the total phase change is proportional to the number of carriers. For example, the penetration depth of 1060-nm light is only several micrometers, and it is completely absorbed within a few tens of micrometers of the modulator, thereby allowing the reflective mode geometry to work to several 10's of gigahertz before velocity mismatch (i.e., bidirectionality) significantly degrades the modulation efficiency (this is similarly true for 1310-nm light in the QWs). However, the carrier effects are often limited by relatively long transit times across the depletion region and the long carrier lifetimes (several nanoseconds).

The green trace in Fig. 11 shows an initial measurement where the optical-optical modulators (Michelson configuration) had a −3-dB bandwidth of just over 100 MHz. The response can be improved by using H^+ ion implantation which introduces damage points and vacancies into the

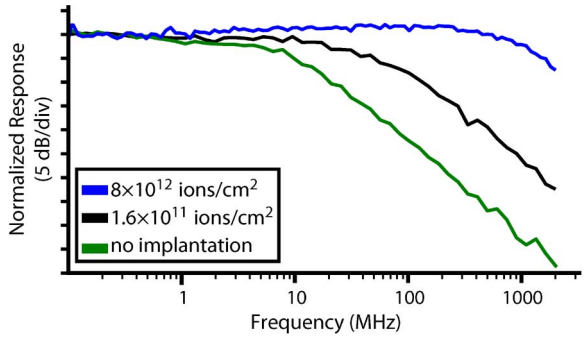

Fig. 11. Measured optical-to-optical modulation response for a Michelson interferometer which shows the bandwidth improvement with H^+ ion implantation. Response is in terms of an optical power ratio.

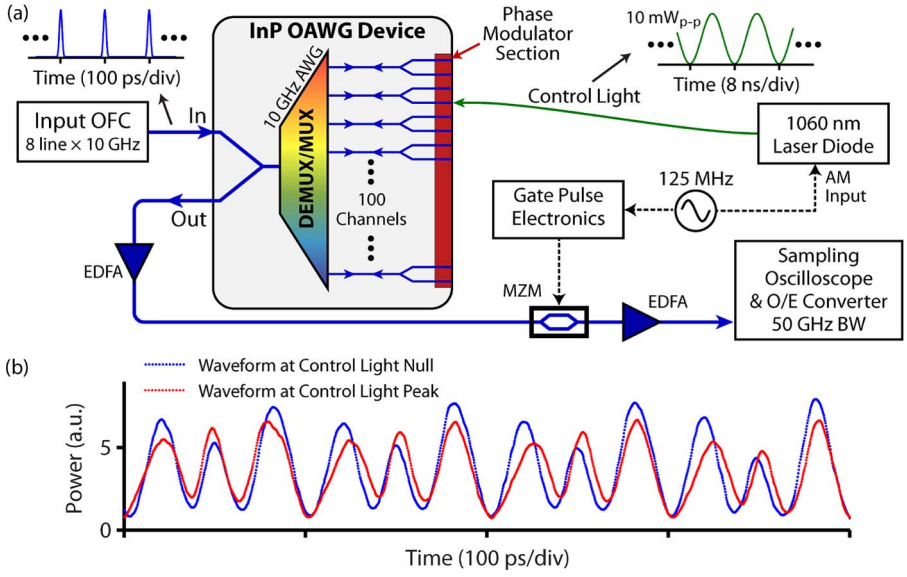

Fig. 12. (a) Experimental arrangement to measure output waveform variation when a channel #75 is modulated with control light. (b) Output waveform intensity where blue and red traces are separated by 4 ns in relative time and correspond to times near the peak and null of the control light.

crystal lattice. These then act as additional recombination centers for free carriers and decrease the carrier lifetime. It has even been shown [20] that the lifetime can be reduced to less than 1 ps at very high doses. Fig. 11 shows that the measured modulation response for sample Michelson interferometer modulators improves to more than 1 GHz for H^+ ion implantation doses of 8×10^{12} ions/cm^2. The modulation bandwidth can be further increased by even larger doses. However, the shorter carrier lifetime does reduce the total number of free carriers, which, in-turn, decreases the modulation efficiency. Thus, an optimal dose is a compromise between modulation efficiency and bandwidth.

To demonstrate an initial dynamically changing arbitrary optical waveform, we launched an eight-line $\times$ 10 GHz input OFC into the OAWG device and optically modulated one arm of the Michelson interferometer on channel #75 [see Fig. 12(a)]. It was not practical to apply H^+ ion implantation to the modulator section of the fully fabricated InP OAWG device due to the metallization layers. Therefore, the optical-to-optical modulation -3-dB bandwidth was limited to just over 125 MHz for reasons discussed previously. As Fig. 12(a) shows, the control light had $\sim$10 mW of peak power and was sinusoidally modulated at 125 MHz. The modulated output waveform was amplified and then time gated to select a 500-ps portion (window) of the modulated waveform for additional

amplification before optical-electrical conversion and measurement by a sampling oscilloscope (50 GHz of optical bandwidth). The gate pulse and oscilloscope trigger had adjustable electrical delays that enabled recording of different portions of the output waveform. Fig. 12(b) shows a 400-ps portion (four periods of the OFC) of the OAWG output waveform intensity at two different relative delays that correspond to a peak or null in the control light. Since only one of the eight optical lines is modulated, we do not expect to see a large change in the output waveform. Yet, there is a distinctive difference between the blue and red waveforms, which are 4 ns apart (one-half the 125 MHz modulation period) in relative time.

The sampling oscilloscope measurement above does not allow retrieval of the spectral amplitude and phase changes. However, as Figs. 8 and 9 showed, the temporal intensity changes in Fig. 12(b) are a good indication of significant spectral modulation (this change is enhanced by using eight comb lines instead of 26). Unfortunately, it was not possible to use the FQSI measurement technique here because it does not acquire such long duration waveforms. Therefore, development of additional waveform measurement techniques is ongoing, and we hope to show full-field output waveform data in a future publication.

5. Conclusion

This paper detailed and demonstrated a monolithically integrated, InP-based OAWG reflection-mode device with access to 1 THz of optical bandwidth. It consisted of a 100-channel × 10-GHz AWG with 100 Michelson interferometers, 200 QW phase modulators, and 400 electrooptic MZMs in twin configurations on a single 50-mm wafer. After phase-error correction, the measured 10-GHz AWG performance was excellent with all 100 output channels present and a −15.1 dB average crosstalk level across the outputs. Measurements demonstrate 20-dB intensity modulation in two regimes: the electrooptic regime by reverse-biasing the QW phase modulators on each channel and the cross-phase modulation regime by injecting 1310-nm optical control light into the QW modulators. An arbitrary waveform created from an 80-GHz wide OFC shows corresponding fluctuations in the output waveform when one line is modulated with 1310-nm control light. Future work includes improving the bandwidth and efficiency of the integrated modulators and reducing the total device loss.

References

[1] K. Takiguchi, K. Okamoto, T. Kominato, H. Takahashi, and T. Shibata, "Flexible pulse waveform generation using silica-waveguide-based spectrum synthesis circuit," *Electron. Lett.*, vol. 40, no. 9, pp. 537–538, Apr. 2004.
[2] Z. Jiang, D. E. Leaird, and A. M. Weiner, "Line-by-line pulse shaping control for optical arbitrary waveform generation," *Opt. Exp.*, vol. 13, no. 25, pp. 10 431–10 439, Dec. 2005.
[3] N. K. Fontaine *et al.,* "32 phase× 32 amplitude optical arbitrary waveform generation," *Opt. Lett.*, vol. 32, no. 7, pp. 865–867, Apr. 2007.
[4] Z. Jiang, C.-B. Huang, D. E. Leaird, and A. M. Weiner, "Optical arbitrary waveform processing of more than 100 spectral comb lines," *Nat. Photon.*, vol. 1, no. 8, pp. 463–467, Aug. 2007.
[5] P. J. Delfyett, S. Gee, H. Izadpanah, S. Ozharar, F. Quinlan, and T. Yilmaz, "Optical frequency combs from semiconductor lasers and applications in ultrawideband signal processing and communications," *J. Lightw. Technol.*, vol. 24, no. 7, pp. 2701–2719, Jul. 2006.
[6] J. T. Willits, A. M. Weiner, and S. T. Cundiff, "Theory of rapid-update line-by-line pulse shaping," *Opt. Exp.*, vol. 16, no. 1, pp. 315–327, Jan. 2008.
[7] M. Akbulut, S. Bhooplapur, I. Ozdur, J. Davila-Rodriguez, and P. J. Delfyett, "Dynamic line-by-line pulse shaping with GHz update rate," *Opt. Exp.*, vol. 18, no. 17, pp. 18 284–18 291, Aug. 2010.
[8] R. P. Scott, N. K. Fontaine, J. P. Heritage, and S. J. B. Yoo, "Dynamic optical arbitrary waveform generation and measurement," *Opt. Exp.*, vol. 18, no. 18, pp. 18 655–18 670, Aug. 2010.
[9] N. K. Fontaine, "Optical arbitrary waveform generation and measurement," Ph.D. dissertation, Dept. Electrical Comput. Eng., Univ. California, Davis, CA, 2010.
[10] N. K. Fontaine, D. J. Geisler, R. P. Scott, T. He, J. P. Heritage, and S. J. B. Yoo, "Demonstration of high-fidelity dynamic optical arbitrary waveform generation," *Opt. Exp.*, vol. 18, no. 22, pp. 22 988–22 995, Oct. 2010.
[11] W. Jiang, F. M. Soares, S. W. Seo, J. H. Baek, N. K. Fontaine, R. G. Broeke, J. Cao, J. Yan, K. Okamoto, F. Olsson, S. Lourdudoss, A. Pham, and S. J. B. Yoo, "A monolithic InP-based photonic integrated circuit for optical arbitrary waveform generation," in *Proc. Conf. OFC/NFOEC*, 2008, pp. 1–3, Paper JTHA39.
[12] S. W. Seo, F. M. Soares, J. H. Baek, W. Jiang, N. K. Fontaine, R. P. Scott, C. Yang, D. J. Geisler, J. Yan, R. G. Broeke, J. Cao, F. Olsson, S. Lourdudoss, A. H. Pham, and S. J. B. Yoo, "Monolithically integrated InP photonic micro systems

on a chip for O-CDMA and OAWG applications," in *Proc. Photon. Switching*, 2007, pp. 97–98, Paper TuP6. [Online]. Available: http://dx.doi.org/10.1109/PS.2007.4300754
[13] N. K. Fontaine, J. Yang, W. Jiang, D. J. Geisler, K. Okamoto, R. Huang, and S. J. B. Yoo, "Active arrayed-waveguide grating with amplitude and phase control for arbitrary filter generation and high-order dispersion compensation," in *Proc. 34th ECOC*, 2008, pp. 1–2. [Online]. Available: http://dx.doi.org/10.1109/ECOC.2008.4729152
[14] F. M. Soares, J. H. Baek, N. K. Fontaine, X. Zhou, Y. Wang, R. P. Scott, J. P. Heritage, C. Junesand, S. Lourdudoss, K. Y. Liou, R. A. Hamm, W. Wang, B. Patel, S. Vatanapradit, L. A. Gruezke, W. T. Tsang, and S. J. B. Yoo, "Monolithically integrated InP wafer-scale 100-channel × 10-GHz AWG and Michelson interferometers for 1-THz-bandwidth optical arbitrary waveform generation," in *Proc. OFC/NFOEC*, 2010, pp. 1–3, Paper OThS1.
[15] S. Jong-In, M. Yamaguchi, P. Delansay, and M. Kitamura, "Refractive index and loss changes produced by current injection in InGaAs(P)-InGaAsP multiple quantum-well (MQW) waveguides," *IEEE J. Sel. Topics Quantum Electron.*, vol. 1, no. 2, pp. 408–415, Jun. 1995.
[16] D. K. Gifford, B. J. Soller, M. S. Wolfe, and M. E. Froggatt, "Optical vector network analyzer for single-scan measurements of loss, group delay, and polarization mode dispersion," *Appl. Opt.*, vol. 44, no. 34, pp. 7282–7286, Dec. 2005.
[17] Y. Suzuki, H. Iwamura, T. Miyazawa, A. Wakatsuki, and O. Mikami, "Polarization-dependent refractive-index change induced by superlattice disordering," *IEEE J. Quantum Electron.*, vol. 32, no. 11, pp. 1922–1931, Nov. 1996.
[18] T. Sakamoto, T. Kawanishi, and M. Izutsu, "Asymptotic formalism for ultraflat optical frequency comb generation using a Mach–Zehnder modulator," *Opt. Lett.*, vol. 32, no. 11, pp. 1515–1517, Jun. 2007.
[19] N. K. Fontaine, R. P. Scott, J. P. Heritage, and S. J. B. Yoo, "Near quantum-limited, single-shot coherent arbitrary optical waveform measurements," *Opt. Exp.*, vol. 17, no. 15, pp. 12 332–12 344, Jul. 2009.
[20] K. F. Lamprecht, S. Juen, L. Palmetshofer, and R. A. Hopfel, "Ultrashort carrier lifetimes in H^+ bombarded InP," *Appl. Phys. Lett.*, vol. 59, no. 8, pp. 926–928, Aug. 1991.